Detection of out-of-time-order correlators and information scrambling in cold atoms: Ladder-*XX* model

Ceren B. Dağ* and L.-M. Duan
Department of Physics, University of Michigan, Ann Arbor, Michigan 48109, USA

(Received 28 August 2018; published 15 May 2019)

Out-of-time-order correlators (OTOCs), recently at the center of discussion on quantum chaos, are tools to understand the information scrambling in different phases of quantum many-body systems. We propose a disordered ladder spin model, the *XX* ladder, which can be designed in a scalable cold atom setup to detect OTOCs with a sign reversal protocol alternative to existing approaches for evolution backward in time. We study both the clean and disordered *XX* ladder and characterize different phases (ergodic and many-body localized phases) of the model based on the decay properties of OTOCs. The emergent effective lightcone shows sublinear behavior, while the butterfly cones drastically differ from the lightcone via demonstrating superlinear behavior. Based on our results, one can observe how the information scrambling changes in the transition from well-studied one-dimensional spin models to unexplored two-dimensional spin models in a local setting.

DOI: 10.1103/PhysRevA.99.052322

Information scrambling has drawn much attention in the last years, not only in gravitational theories to study the information properties of black holes [1–4] but also in quantum many-body physics [5–14]. Even though the initial interest in scrambling was to study quantum chaos in models with gravity duals, information scrambling, first, is not limited to systems with duals and, second, provides an understanding about the dynamics of any generic many-body system. Besides being a complementary approach to level statistics [15] in the context of quantum chaos, the way that the systems scramble information in time can dynamically reveal the properties of a Hamiltonian in an experiment. The tool to measure the information scrambling is a correlation function, the so-called out-of-time-order correlator (OTOC). The physics that the OTOC captures is the growth of the commutator of two operators in time and this growth can be characterized by

$$C_i^{\beta}(t) = -\frac{1}{Z}\mathrm{Tr}\{e^{-\beta H}[A_i(t), B_{j=0}]^2\} \tag{1}$$

for a system with a finite inverse temperature β. Here i denotes a site in the lattice, $j = 0$ is the first lattice site, $A_i(t)$ and $B_{j=0}$ are local Hermitian operators for their corresponding sites, and Z is the partition function. The local observables of two sites at a distance initially commute, but the interactions lead the system to become more correlated in time, and the buildup of the correlations between sites at a distance starts to be seen in the Heisenberg operators that no longer commute. Therefore, the initially localized operators spread across the space dimension and become as nonlocal as possible around the scrambling time. OTOCs are sensitive to conserved quantities [5,16,17], revealing the (non)integrability of the system; they also show the signatures of localized phases [5–9], equilibrium [18] and dynamical phase transitions [10], chaotic properties of thermal systems [4,13,19], e.g., exponential decay in OTOCs, and finally the (non-)locality and information transport of the Hamiltonian via emergent lightcones [11–14]. All these theoretical discoveries on OTOCs call for experimental proposals and experiments in order to probe and eventually utilize scrambling.

To date, there have been a number of experimental proposals [13,20–24] and realizations [16,25,26] on scrambling detection. In this paper, one of our aims is to come up with the simplest possible cold atom setup that shows a wide range of diverse scrambling phenomena and could pave the way to the scalable OTOC measurements of nonintegrable spin systems. The cold atom setup is a realistic candidate to probe OTOCs, mainly due to scalability and its weak coupling to the environment [27,28]. Information scrambling could be induced by environment effects as well, and therefore it is important to differentiate the scrambling due to correlation built up via many-body interactions in an experiment [26]. The scalability of cold atoms could be utilized to increase the size and hence the duration of transient effects in OTOCs by delaying the saturation stage. The most crucial step of OTOC measurement is the evolution backward in time. We propose a sign reversal mechanism as an alternative to existing approaches. The conventional solution to reverse the sign of a cold atom Hamiltonian is to utilize Feshbach resonances [13,29]. We will show that a sequence of single-spin gates can be performed via fast laser pulses [30,31] to measure the OTOCs.

In the first section, we explain our model and its cold atom setup. Then we systematically study the level statistics and scrambling properties of *XX* ladders both with and without disorder. In the final part, we lay out the scrambling detection with an experimental initial state preparation.

*cbdag@umich.edu

I. THE LADDER-XX MODEL

Ladder spin models have been studied to explore their critical phenomena [32–34] and entanglement properties [35]. They are seen as useful intermediate models to understand the magnetic properties of materials while increasing the dimension from d to $d+1$ [36]. There are also natural cuprate compounds that are modeled by ladder spin models at $d=1$ [34] and they have been considered as candidate models to explain high-T_c superconductivity [37]. More recently ladder spin models are studied in the context of transport [38]. We set our chaotic ladder model as the ladder-XX model because of its simplicity in cold atom realization:

$$H = \sum_{j=1,2}\sum_{i=1}^{L-1} J_{\parallel}\left(\sigma^x_{j,i}\sigma^x_{j,i+1} + \sigma^y_{j,i}\sigma^y_{j,i+1}\right) + \sum_{i=1}^{L} J_{\perp}\left(\sigma^x_{1,i}\sigma^x_{2,i} + \sigma^y_{1,i}\sigma^y_{2,i}\right) + \sum_{i=1}^{L} h_i\left(\sigma^z_{1,i} + \sigma^z_{2,i}\right), \quad (2)$$

with random disorder h_i which is drawn from a uniform distribution with disorder strength of $[-h, h]$. $\sigma^{x,y,z}$ are Pauli matrices for the spin-1/2 system, $J_{\parallel}$ is the intrachain hopping coefficient, and $J_{\perp}$ is the rung hopping coefficient. L is the system size for a single chain and we go up to $L=8$ in our numerical analysis with exact diagonalization.

The ladder-XX model could be realized at the hard-core boson limit of the Bose-Hubbard model [39,40]. At the hard-core boson limit with $U\to\infty$ and a noninteger filling factor that implies every site has either zero or one boson, we end up with a superfluid Hamiltonian $H_{U\to\infty} = -t_{\parallel}\sum_{i,i+1}(a_i^{\dagger}a_{i+1} + \text{H.c.}) - \sum_i \mu_i a_i^{\dagger}a_i$, that can easily be mapped to the XX chain via mapping the annihilation operator to the spin lowering operator $a\to\sigma^-$ and via mapping the creation operator to the spin raising operator $a^{\dagger}\to\sigma^+$. The mapping leads us to have $J_{\parallel}=2t_{\parallel}$, $J_{\perp}=2t_{\perp}$ and the random chemical potential is mapped to random magnetic field strengths $\mu_i = h_i$ via $a_i^{\dagger}a_i - 1/2 \to \sigma^z$. Therefore, we can recover Hamiltonian Eq. (2) with two interacting Bose-Hubbard chains exposed to random chemical potential in the hard-core boson limit. The boson state vectors correspond to either spin down $|\downarrow\rangle$ or spin up $|\uparrow\rangle$ in the ladder-XX model. Since the filling factor is fixed in the cold atom scheme, the corresponding case in our spin model [Eq. (2)] has fixed total spin S_z. We set the filling factor $f=0.5$ and the OTOC of the system is studied at the subsector $S_z=0$.

We utilize superlattices to create random disorder in the Bose-Hubbard chains [41,42] and to let two chains interact with each other. For the latter, we create a double-well potential via choosing the laser frequencies as k and $2k$ in the y direction with a phase difference between them ϕ, e.g., $V_y(y) = V_{1y}\sin^2(k_y y) + V_{2y}\sin^2(2k_y y + \phi)$, assuming $V_{1y}\sim V_{2y}$ so that the bosons can be trapped in the double-well potential. For the random disorder, we interfere two optical fields with incommensurate frequencies, e.g., $V_x(x) = V_{1x}\sin^2(k_{1x}x) + V_{2x}\sin^2(k_{2x}x)$, where $k_{1x}/k_{2x}\in \mathbb{R}/\mathbb{Q}$ for both of the chains. When $V_{2x}\ll V_{1x}$, the disorder lattice can simulate the true random potential [41,42]. One can tune the hopping coefficients $J_{\parallel}$ and $J_{\perp}$ in the ladder-XX model through the laser amplitudes and frequencies [39] and thus access different OTOC behaviors with the simulation time of $t\propto 1/J_{\parallel}\propto$ 1–10 ms in laboratory. Therefore, the measurement time of the OTOC is in the limits of cold atom experiments [43].

II. THE OTOC PROPERTIES AND LEVEL STATISTICS

For a spin system Eq. (1) can be recast to the OTOC, by first setting the temperature infinite, $\beta\to 0$, and then noting that

$$F_i^{\text{ex}}(t) = 1 - \frac{C_i^0(t)}{2N}, \quad (3)$$

where $C_i^0(t) = \|[\sigma_i^z(t), \sigma_1^z]\|_F^2$. Since the Pauli matrices are Hermitian, norm 2 (the Frobenius norm) could be utilized to rewrite Eq. (1). N is the dimension of the Hilbert space and the superscript "ex" stands for the exact value of the out-of-time-order correlator. Equation (3) is measurable given that a $\beta=0$ initial state is prepared. In general, calculating an expectation value with respect to the infinite-temperature state requires averaging over all eigenstates. However, we can approximate the OTOC Eq. (3) with smaller number of states:

$$F_i^{\sim}(t) = \sum_j \langle\psi_j|\sigma_i^z(t)\sigma_1^z\sigma_i^z(t)\sigma_1^z|\psi_j\rangle, \quad (4)$$

where $|\psi_j\rangle$ denotes a pure random initial state (or a mixture of random initial states) drawn from the Haar measure [11]. Haar random states are typically maximally entangled states within a small error [44]. The error of approximating a $\beta=0$ initial state is exponentially suppressed as the Hilbert space increases via typicality arguments [45,46]. This procedure is numerically less expensive compared to other methods for preparing the initial state at $\beta=0$, even though the Haar random states are hard to generate experimentally [47]. The results presented in this paper are based on averaging over more than one random initial state to obtain the OTOC as precise as possible (see Appendix B for error bounds).

When a generalized form of Jordan-Wigner transformation [48] is applied, the XX ladder can be shown to be interacting in the spinless fermion representation. Therefore we expect to see ergodic to many-body localized (MBL) phase transition in this model [49,50]. A common way to determine if a quantum system is chaotic is via the energy-level statistics [15,49–51]. Energy-level spacings are $\delta_\gamma^n = |E_\gamma^n - E_\gamma^{n-1}|$ where E_γ^n is the corresponding energy of the many-body eigenstate n in a Hamiltonian of disorder realization γ. Each γ represents a different set of random disorder h_i drawn from uniform distribution. Then we can calculate the ratio of adjacent gaps as $r_\gamma^n = \min(\delta_\gamma^n, \delta_\gamma^{n+1})/\max(\delta_\gamma^n, \delta_\gamma^{n+1})$ as the indicator of the level statistics [49,50]: $r_\gamma^n \sim 0.53$ and 0.39 are representative of Wigner-Dyson and Poisson statistics, respectively. If the distribution of the energy-level spacings follows Wigner-Dyson statistics through a generalized orthogonal ensemble (GOE) distribution, the model shows ergodic behavior, whereas Poisson statistics imply a localized phase [15,51]. Figure 1 shows the average ratio values $\langle r_\gamma^n\rangle_{\gamma,n}$ varying between random field strengths of $h=0$ and 10 for different system sizes ranging between $L=4$ and 8 when they are averaged over 5×10^3 to 10 different random samples. The average of r_γ^n over a set of different Hamiltonians H_γ and eigenstates n

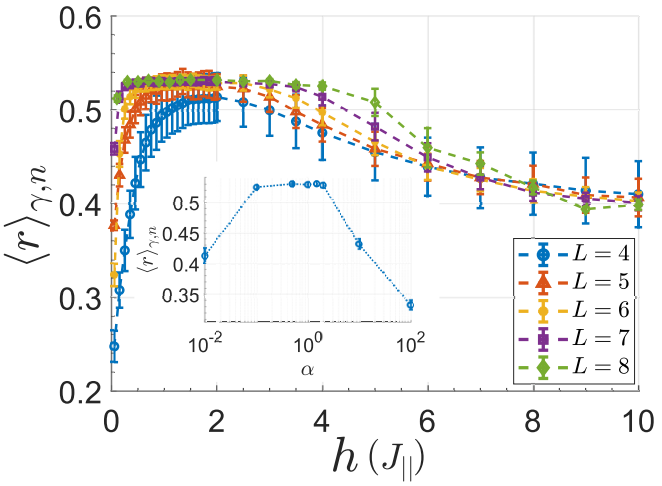

FIG. 1. The average ratio of level spacings $\langle r_\gamma^n \rangle_{\gamma,n}$ with respect to disorder strength h. Coupling strengths are set to $J_\perp = J_\parallel$ and $\langle r_\gamma^n \rangle_{\gamma,n}$ is averaged over 5×10^3 to 10 random realizations for single-chain sizes ranging between $L = 4$ and 8. Inset: $\langle r_\gamma^n \rangle_{\gamma,n}$ at $h = 1\,[J_{||}]$ with respect to rung interaction strength α where $J_\perp = \alpha J_\parallel$ for $L = 7$.

converges to $\langle r_\gamma^n \rangle_{\gamma,n} \sim 0.53$ in the presence of small disorder strength $h \lesssim 3\,[J_{||}]$, hence implying an ergodic phase. As $h \gtrsim 9\,[J_{||}]$, we observe $\langle r_\gamma^n \rangle_{\gamma,n} \sim 0.39$, which indicates a MBL phase.

Figure 2 shows how the OTOC of σ_1^z and σ_7^z for the $L = 7$ chain changes with respect to the rung interaction strength. At the limit of $\alpha = J_\perp/J_\parallel \to 0$, the system converges to two independent XX chains with random disorder, whereas the opposite limit of $\alpha \to \infty$ implies a dimer phase as another integrable limit of the XX ladder. In both cases, the

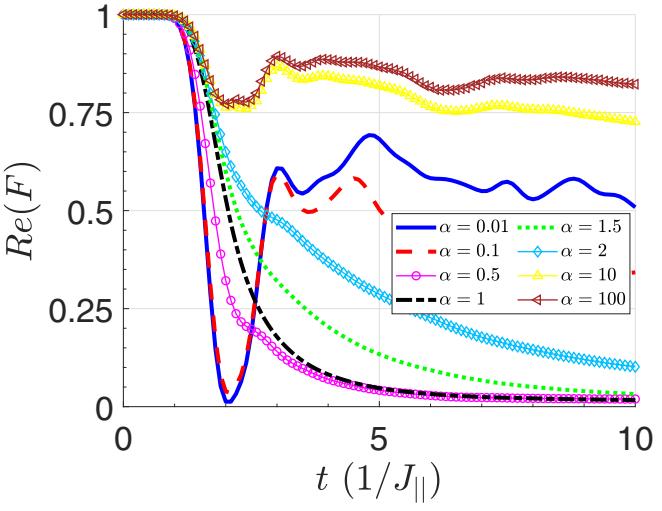

FIG. 2. The OTOC of the ladder-XX model at $h = 1\,[J_{||}]$ between two distant operators σ_1^z and σ_7^z in the first chain with respect to α for $L = 7$. $\alpha \sim 1$ corresponds to the interacting limit, whereas the cases $\alpha \ll 1$ and $\alpha \gg 1$ are integrable limits of the ladder-XX model. The OTOC is averaged over 100 different random samples. The plot shows the mean values (see Appendix A for the error bars on the curves).

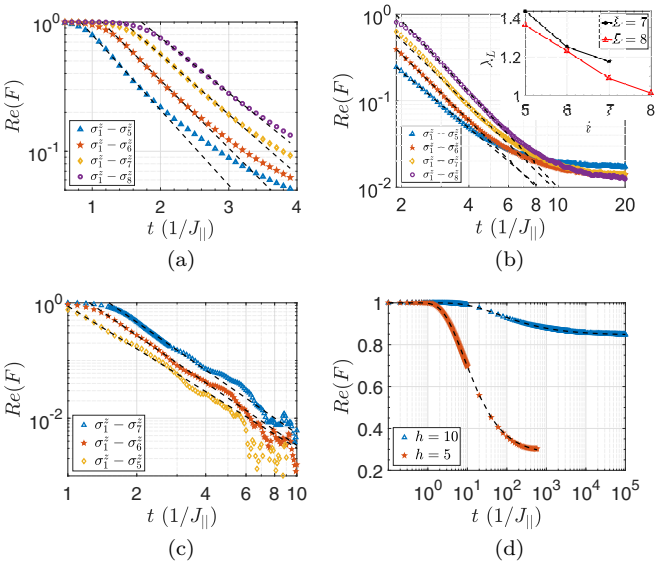

FIG. 3. (a) The exponential and (b) power-law decay of OTOCs for σ_1^z with σ_5^z (blue triangles), σ_6^z (red pentagrams), σ_7^z (orange diamonds), and σ_8^z (purple circles) observables in a system size of $L = 8$. The inset in (b) shows the Lyapunov-like exponent extracted from exponential fitting for both $L = 7$ (black asterisks) and $L = 8$ (red triangles). (c) No disorder case: Only power-law decay of OTOCs for σ_1^z with σ_5^z (orange diamonds), σ_6^z (red pentagrams), and σ_7^z (blue triangles) observables when $L = 7$ and $h = 0$. (d) Crossover region with $h = 5\,[J_{||}]$ (red pentagrams) and MBL with $h = 10$ (blue triangles) for observables $\sigma_1^z - \sigma_7^z$ with $L = 7$.

corresponding fermion representation becomes noninteracting, and hence points to single-particle dynamics with Anderson localization [5,9]. We see a permanent revival after a decay and larger oscillations in the OTOC as observed in integrable systems [16,19]. In addition, the average level spacing ratio $\langle r_\gamma^n \rangle_{\gamma,n}$ decreases from ∼0.53 to ∼0.39, thus demonstrating level statistics for integrable systems (see inset of Fig. 1). We note that the OTOC for $\alpha \to \infty$ scrambles less than the OTOC for $\alpha \to 0$ with a small initial decay, since the model also becomes weakly coupled throughout the x dimension in this limit. The OTOC decays rapidly in the interacting limit around $\alpha \sim 1$ and saturates at $F(t \to \infty) \sim 0$ while showing GOE distribution with $\langle r_\gamma^n \rangle_{\gamma,n} \sim 0.53$ and hence quantum chaos in its energy levels. We set $\alpha = 1$ for the rest of our paper and study the interacting limit.

The chaotic regime of the ladder-XX model ($h = 1\,[J_{||}]$) demonstrates a brief interval of exponential decay in early-time dynamics [Fig. 3(a)], followed by power-law tails [Fig. 3(b)] before entering into the saturation regime. The inset in Fig. 3(b) shows the Lyapunov-like exponents extracted from the data both for $L = 8$ and 7 (Appendix C) when we fit $\mathrm{Re}(F) = a\exp(-\lambda t)$ to the data, where a is a constant. Quantum chaotic models are expected to scramble the information fast and hence show exponential decay of the OTOC [4] before the saturation. Exponential decay is a transient feature of systems with finite size and bounded operators [52], a result we observe in Fig. 3(a). The Bose-Hubbard model [13] and time-dependent systems [5,53] were shown to decay exponentially, whereas it is numerically hard to show the exponential

decay in time-independent quantum chaotic spin chains, e.g., the disordered Heisenberg model [5]. In fact, the transient exponential decay turns into power-law decay $\mathrm{Re}(F) = at^{-b}$ in Fig. 3(b) for the ladder-XX model, thus reminding us of the quasiexponential generic form put forward by [14]. When there is no disorder, Fig. 3(c), a decay with power-law trend is observed. There are significantly larger oscillations around the saturation value in the clean limit, however in both clean and disordered cases the scrambling time is approximately the same. For a comparison, the power-law exponents for disordered and clean cases are $b = 2.65$ and 2.76, respectively, for the observables $\sigma_1^z - \sigma_7^z$ in a system with $L = 7$. The ladder-XX model has energy and spin conservation, similar to the Heisenberg model where the OTOC has been observed to be sensitive to conserved quantities and show power-law decay [5]. In addition to that, the XX ladder has invariant subspaces that show ballistic transport but are not associated with local conserved quantities at the same time, hence the energy levels still show quantum chaos [38]. When random disorder is introduced, these invariant subspaces can support Anderson localized eigenstates regardless of the disorder strength [54]. We first conclude that the invariant subspaces do not change the power-law decay, however they affect the saturation value of the OTOC. Figures 3(b) and 3(c) show that the saturation value is much higher both in disordered $F(t \to \infty) > 10^{-2}$ and clean $F(t \to \infty) > 10^{-3}$ limits, compared to other models such as Heisenberg and transverse-field Ising models of similar sizes $F(t \to \infty) \sim 10^{-5}$ [5]. Further, we notice that the saturation value of the OTOC becomes even larger when the disorder is introduced. Even though the disorder clearly resolves the degeneracies caused by symmetries, the disordered system scrambles less than the clean system. Thus, we point to Griffiths rare-region effects [55] that might also be responsible for turning exponential decay in early time into a power law later in time.

The decay becomes even slower as we increase the disorder strength h, Fig. 3(d). The system shows no scrambling for a time interval of $t \sim 10[1/J_{||}]$ when $h = 10\,[J_{||}]$ and differs from the OTOC at $h = 5\,[J_{||}]$ that is at the crossover region in Fig. 1. Even though for short times it looks like Anderson localization, simulation over long times reveals an MBL-like decay by showing a clear signature of logarithmic decay at intermediate times for both $h = 5$ and 10. By slightly modifying the general form given in Ref. [7] for logarithmic MBL decays, we find that the decay profiles in Fig. 3(d) could be fitted to $\mathrm{Re}(F) = 1 - a\exp(-bt^c)$, where the parameter a determines the saturation value, and $c < 0$ for the OTOC to decay as $t \to \infty$ and $F = 1$ as $t \to 0$. Similarly this form reduces to logarithmic decay, $\mathrm{Re}(F) \sim 1 - \frac{a}{e} + \frac{a\times c}{e}\log(b^{1/c}t)$ for $b^{1/c}t \sim 1$. The fit parameters read $a = 0.725$, $b = 5.727$, $c = -0.812$ for $h = 5$ and $a = 0.154$, $b = 8.661$, $c = -0.519$ for $h = 10\,[J_{||}]$. Therefore, the logarithmic decay is valid around $t \sim 10\,[1/J_{||}]$ and $t = 10^2\,[1/J_{||}]$ for $h = 5\,[J_{||}]$ and $10\,[J_{||}]$, respectively. One can further see that Anderson localization lies in the limit $|c| \to 0$, which implies logarithmic decay should happen when $t \to \infty$, meaning that the OTOC does not decay at all. As a result, we demonstrate that there could be intermediate cases where the OTOC does not decay to zero, but to finite nonzero values in the MBL phase, which is possibly related to atypical eigenstates in XX ladders [54].

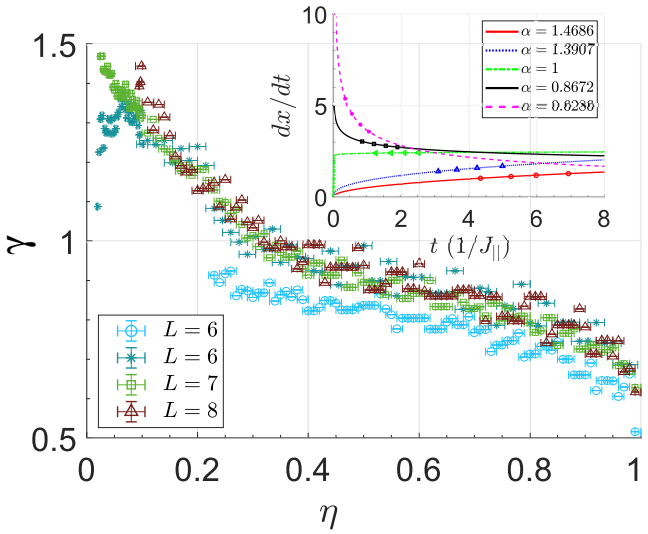

FIG. 4. The dynamical exponent γ with respect to the OTOC contour values η extracted from analyzing data sets for $L = 6$ with observables from σ_2^z to σ_6^z (light blue circles), with observables from σ_4^z to σ_6^z (dark blue stars), $L = 7$ from σ_4^z to σ_7^z (green squares), and $L = 8$ from σ_4^z to σ_8^z (red triangles) for a random disorder strength of $h = 1$. We averaged the data over 2×10^2, 1×10^2, 1×10^2, and 1×10^1 times for the first two $L = 6$, 7, and 8 system sizes, respectively. Inset: The rates of the sublinear, linear, and superlinear wavefronts for a system size of $L = 7$. The markers are the data points, while the lines are the differentiations of the wavefront curves.

In a lightcone figure (Fig. 5), each point has a set of discrete space x and time t coordinates, where the space dimension is emergent due to the nearest-neighbor couplings and defined as the distances between lattice sites in the lower leg of the ladder. The value of a point is the OTOC, denoted as η. If we follow the OTOC contours composed of the same η value, we obtain a series of space-time coordinates that give us a wavefront [11,12,56,57]. A couple of wavefronts associated with different η values ranging between $\eta = 1$ and 10^{-2} are shown in Fig. 5. These wavefronts are expected to present how the correlations spread in the system over time. The outermost wavefront $\eta \sim 1$ corresponds to the lightcone, while $\eta \sim 0$ corresponds to the butterfly cone in the literature [58]. The wavefronts that we extracted follow the power law: $x \sim t^\gamma$ where γ is dubbed as the dynamical exponent. Figure 4 shows a range of γ changing from the low end of $\sim$0.5 to the high end of $\sim$1.5 with respect to η for different system sizes. It is not clear if γ would have a maximum in Fig. 4 due to the limitations in the data. We find a sublinear lightcone with $\gamma < 1$ where the spread is sub-ballistic. This observation aligns with the rare-region effects [55]. On the other hand, as the system scrambles, we observe that the wavefronts first become linear $\gamma = 1$ and then pass to a superlinear region $\gamma > 1$ in Fig. 4(a). Therefore, the butterfly cones at $\eta \sim 0$ seem to differ significantly from the lightcone at $\eta \sim 1$. The wavefront structures that demonstrate the superlinear butterfly cones can be seen in Fig. 5(a). We plot the rates of the wavefronts in the inset of Fig. 4 where the sublinear lightcone ($\eta = 0.99$) initially bounds the rest. Towards the scrambling time, the linear wavefront ($\eta = 1$) seems to be the new bound on the wave-

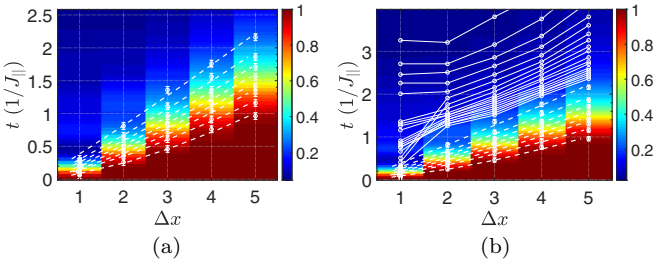

FIG. 5. A demonstration of wavefronts for a system size of (a) $L = 8$ and (b) $L = 6$, where the x axis and y axis are the distance and time, respectively. (a) The fitted wavefronts change from sublinear to superlinear in time between the displacements $\Delta x = 3$ and 7 units. (b) Only the sublinear wavefronts are fitted between $\Delta x = 1$ and 5 units (dotted lines), while the solid lines show irregular wavefronts appearing later in time.

front rates. A range of sublinear wavefronts were detected in the disordered Heisenberg chain before [11], implying the lightcone still differs from the butterfly cones in the dynamical exponent. Superballistic spread of correlations ($\gamma > 1$) has been previously observed in one-dimensional (1D) spin chains with power-law decaying long-range interactions [12,56,57]. The ladder models can always be mapped to a path that passes through all the sites, e.g., zigzag or meander paths, so that 1D Jordan-Wigner transformation can be applied [59]. Such mappings bring long-range interactions due to the Jordan-Wigner strings, which could explain the super-ballistic spread appearing later in time. We note that its rate remains insignificant compared to the faster wavefronts. It is an interesting direction to see if other ladder models present similar wavefront structures. Finally, we demonstrate the irregular wavefronts appearing in the spatial region [60] when the displacement is $\Delta x = 1$–2 in Fig. 5(b). The only fitted wavefronts are the sublinear wavefronts shown in Fig. 5(b) as dotted white lines, because the wavefronts start to exhibit irregularities later in time (solid white lines). The irregularity appears between the origin and two sites away from it, as we observe that it takes significantly greater time for the information to spread $\Delta x = 2$ units compared to $\Delta x = 1$ unit in the time interval of $t \sim 0.5\,[1/J_{||}]$ to $t \sim 2\,[1/J_{||}]$. Hence it seems that the information spread slows down locally and temporarily [the jump feature in Fig. 5(b)] before showing a sub-ballistic trend for $\Delta x > 2$. Furthermore, after $t \sim 2\,[1/J_{||}]$ the jump feature is replaced by a constant line between $\Delta x = 1$ and 2 units, which points to a locally scrambled region in the ladder while the information still spreads in the rest of the system at a finite rate. This unusual region-restricted scrambling continues until the whole ladder completely scrambles. Therefore, we conclude that different rare-region effects are at play in the ladder XX, which calls for a more systematic future study.

III. OTOC DETECTION PROTOCOLS

The scrambling in the ladder-XX model can be detected via the interference measurement scheme on many-body states in optical lattices [61,62] or the interferometric measurement scheme [20]. We detail both measurement schemes in the following subsections and elaborate on their advantages and disadvantages. Since both schemes need an experimental initial state preparation, we first focus on how to design an initial state that would sufficiently approximate an infinite-temperature state.

A. Initial-state preparation

One can ideally use the whole set of Fock states to create a $\beta = 0$ initial state. However, given that this process would be lengthy, we ask if using a few ($M \ll N$) randomly chosen Fock states would sufficiently mimic $\beta = 0$ initial state $\mathbb{I} \sim \sum_{j=1}^{M} |\psi_j\rangle\langle\psi_j|$, where $|\psi_j\rangle = \{|\binom{1\ldots}{0\ldots}\rangle, \ldots, |\binom{0\ldots}{1\ldots}\rangle\}$ are Fock states for the ladder and they span the Hilbert space at half filling. We find out that initiating an experiment with a randomly set Fock state for ~ 10 or $\sim 10^2$ times mimics the $\beta = 0$ state up to a mean error of $\sim 7 \times 10^{-3}$ or 2×10^{-3}, respectively, for a system size of $L = 6$ [Fig. 6(e)]. We study how the mean error scales with the sampling ratio M/N in Figs. 6(a) and 6(b) for different system sizes. Here the mean of the error is calculated for the data points when the error signal $\epsilon_1(t) = |F^{\text{ex}}(t) - \frac{1}{M}\sum_j F_j(t)|$ saturates in time. The sampling ratio M/N has bounds $0 < M/N < 1$ and we observe when $M/N \gg 0$ the scaling is exponential and the data for all simulated system sizes could be collapsed to a single decay exponent $b \sim -2.5$ in $\epsilon_1(t) \propto a\exp(-bM/N)$ [see Fig. 6(a)]. Note that when $M/N = 1$, meaning that all Fock states are used, the error is zero up to machine precision and the OTOC is exact, and the point $M/N = 0$ is not well defined. Except for small sizes, e.g., $L = 3$, the observed exponential scaling in Fig. 6(a) is not experimentally practical due to the increasing number of randomly sampled Fock states. Therefore, we study the limit $M/N \to 0$ separately where we obtain power-law scaling in M/N [see Fig. 6(b)] with $b \sim -0.5$ in $\epsilon_1(t) \propto a(M/N)^b$ for system sizes $L = 4$–7.

Remarkably, it is possible to bound the error of approximation to $\sim 10^{-2}$ with only one Fock state for $L = 7$. In fact the error decreases as a power law with the increasing system size when only one Fock state is used to mimic the infinite-temperature state [Fig. 6(c)]. Figure 6(c) shows nine different realizations of using only one randomly set Fock state and a single power-law curve fitted to all with $b \sim -2.26$ in $\epsilon_1(t) \propto (2L)^b$ (Appendix D). This observation is not utterly surprising, because a Fock state has a broad eigenstate occupation number (EON) distribution [Fig. 6(d) and Appendix D]. An EON distribution $|c_\beta|^2$ can be defined as the overlap of the initial state with the eigenbasis of the time-evolving Hamiltonian: $|\psi(0)\rangle = \sum_\beta c_\beta|\psi_\beta\rangle \to |c_\beta|^2$, where ψ_β are the eigenstates and $|\psi(0)\rangle$ is the initial Fock state. For instance, an infinite-temperature state has a uniform EON distribution: $|c_\beta|^2 = 1/N$. To be more precise, we can calculate the so-called effective dimension of the initial state, $d_e = (\sum_\beta |c_\beta|^4)^{-1}$ [63,64], and study the scaling of the effective dimension with the dimension of the Hilbert space. For an infinite-temperature state, $d_e = aN^\xi$ with an exponent of $\xi = 1$ and $a = 1$, which should be compared with the scaling exponent for the effective dimension of a randomly set Fock state. Figure 6(d) shows the data collapse on the effective dimensions of ten different randomly set Fock states for each system size. The fit parameters $d_e \sim 0.3N$ show that a randomly set Fock state also gives an exponent $\xi = 1$, which more accurately demonstrates the broadness

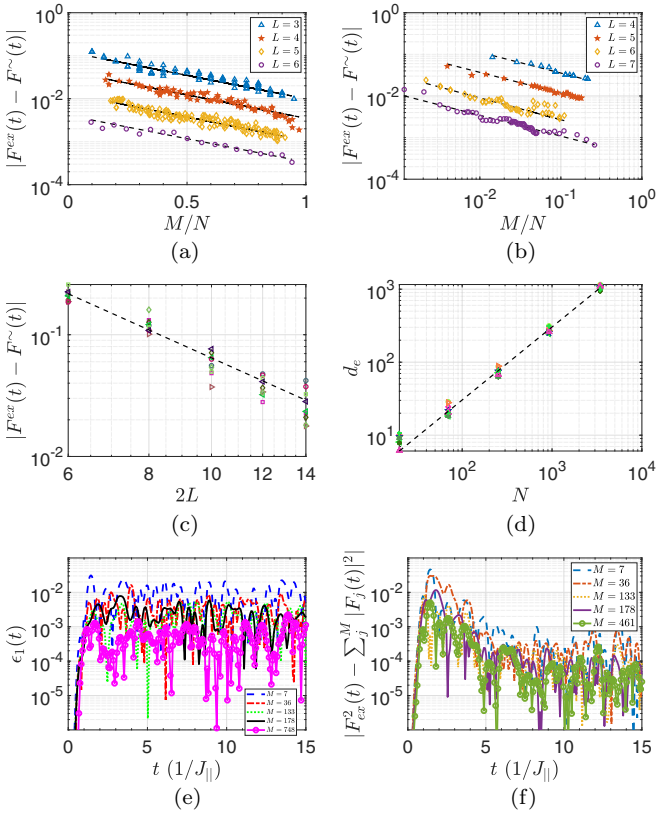

FIG. 6. Initial-state preparation at $h = 1\,[J_{||}]$. (a) The scaling of the mean error $\epsilon_1(t)$ with respect to M/N sampling ratio, where M and N are the number of randomly sampled states and the dimension of the Hilbert space, respectively. The blue triangles, red pentagrams, orange diamonds, and purple circles stand for a single-chain size of $L = 3$ to 6, where all have an exponent of $b \sim -2.5$ in the fit $\propto a\exp(-bM/N)$. (b) The scaling of the mean error for small M/N ratio has power-law scaling $\propto a(M/N)^b$ with $b \sim -0.5$ for all system sizes of $L = 4$ (blue triangles), $L = 5$ (red pentagrams), $L = 6$ (orange diamonds), and $L = 7$ (purple circles). (c) The data collapse applied to the scaling of the mean of the error $\epsilon_1(t)$ with respect to the system size for only one randomly sampled Fock state. Each data point is a random realization where the fitted curve gives an exponent of $b \sim -2.26$ in $\epsilon_1(t) \propto (2L)^b$. (d) The scaling of the effective dimension d_e with the Hilbert-space size, N, gives linear scaling $d_e = 0.3N$, mimicking an infinite-temperature state. (e) The error signal $\epsilon_1(t)$ with respect to time, for an average of $M = 7$ (blue dashed), $M = 36$ (red dash dotted), $M = 133$ (green dotted), $M = 178$ (black solid), and $M = 748$ (pink circles) randomly sampled Fock states. (f) The error signal $\epsilon_2(t) = ||F^{\rm ex}(t)|^2 - \frac{1}{M}\sum_j^M |F_j(t)|^2|$ with respect to time, for an average of $M = 7$ (blue dashed), $M = 36$ (red dash dotted), $M = 133$ (orange dotted), $M = 178$ (purple solid), and $M = 461$ (green circles) randomly sampled Fock states. Both (e) and (f) have a system size of $L = 6$.

of the EON distribution. The coefficient in front is bounded for effective dimension scalings, $a \leqslant 1$, and we see that a randomly set Fock state has $a \sim 0.3$. This reflects the fact that the Fock state does not show uniform distribution in the eigenbasis of the Hamiltonian, and hence we have a nonzero error signal $\epsilon_1(t)$.

In conclusion, we see that the exact shape of the EON distribution is insignificant as $L \to \infty$, as long as it is a broad

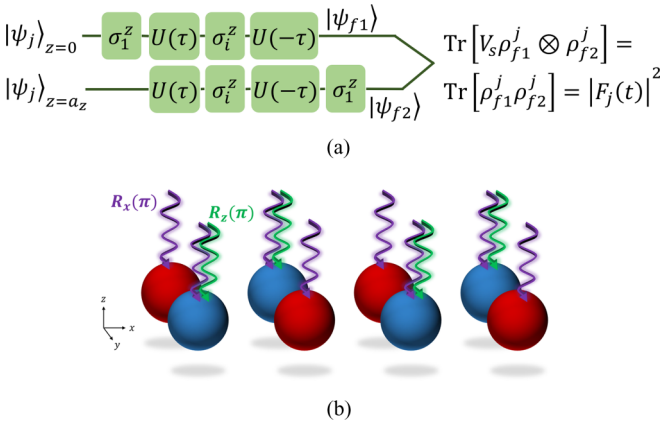

FIG. 7. (a) The schematic that illustrates the circuit for OTOC measurement with the spin operators σ_1^z and σ_i^z. The circuit utilizes interference measurements providing $\mathrm{Tr}\{|\psi_{f1}\rangle\langle\psi_{f1}|\,|\psi_{f2}\rangle\langle\psi_{f2}|\} = |F_j(\tau)|^2$. (b) Schematic for Hamiltonian sign-reversal protocol for evolution backwards in time: red and blue spheres stand for spin-up and -down states, respectively. We simultaneously perform $R_z(\pi)R_x(\pi)$ gates for the odd-numbered spins in the first leg and even-numbered spins in the second leg, while only one gate $R_x(\pi)$ is applied to the rest of the spins. $R_z(\pi)$ and $R_x(\pi)$ are denoted by green and purple wiggly lines, meaning that the single-spin gates for cold atom systems could be realized via laser pulses [31,66] or microwaves [67].

distribution in the eigenbasis. Therefore, only one Fock state could approximate the infinite-temperature OTOC reasonably well. We note that our analysis is valid for $h = 1\,[J_{||}]$ disorder strength. The observation that a single Fock state could exhibit $\xi = 1$ exponent in its effective dimension scaling is possibly related to the extended eigenstates existing throughout the spectrum in the chaotic regime. Hence, whether the found power-law scaling in system size for a single Fock state as well as the exponential and power-law scalings of the error in the sampling ratio M/N depend on the disorder strength is an interesting question for future studies and experiments. Our results also show that a few randomly sampled Fock states could be used as an alternative approach to Haar-distributed random states in numerics to calculate the OTOC with a $\beta = 0$ initial state at the chaotic regime of a model.

B. The interference measurement

$|F(t)|^2$ is the quantity to measure in the interference measurement scheme [61]. We see that $\mathrm{Im}[F(t)] \sim 0$ and $\mathrm{Re}[F(t)] \geqslant 0$ throughout the simulation time with the parameters used in the paper, thus rendering $|F(t)|^2$ a good quantity to measure. The interference measurement scheme has been proposed to probe scrambling in the Bose-Hubbard model previously [13,65], however note that the implementation of the interference measurement further simplifies for the hard-core boson limit [61] which we utilize in the cold atom setup of our model. The steps of the interference detection protocol are as follows [Fig. 7(a)].

(i) Generate two copies of the same randomly sampled Fock state $|\psi_j\rangle$: We can first set a two-dimensional (2D) lattice to Mott-insulator phase with unit filling factor and then adiabatically ramp the lattice potential to a double-well

potential at each site in the y direction. This would produce a $(|10\rangle + |01\rangle)/\sqrt{2}$ state for a double well, and via suppressing the tunneling between wells in the double wells one can generate randomly sampled Fock states in 2D lattice at half filling. To make two copies of the initial state, we can introduce another lattice layer in the z direction and apply the same operations of the lattice potential simultaneously for both planes.

(ii) Apply the $\sigma^z_{1,1}$ gate on the first spin in the lower leg in the first copy.

(iii) Apply to both copies $U(\tau)\sigma^z_{1,i}$, where $U(\tau)$ is evolution forward in time for τ and the σ^z_i gate is applied to any spin i further away from the first spin in the lower leg.

(iv) Hamiltonian sign reversal protocol: As illustrated in Fig. 7(b), we apply a set of gates to the lattice sites simultaneously to change the overall sign of the Hamiltonian so that we can evolve the many-body state with $-H$. Given that we shine either laser pulses [31,66] or microwaves [67] to implement single-spin rotations, our protocol of Hamiltonian sign reversal could be related to nuclear magnetic resonance Hamiltonian engineering [16,23], though with a difference of site-resolving pulses in the cold atom setup. Remembering $R^\dagger_z(\theta)\sigma^x R_z(\theta) \to \cos\theta\sigma^x - \sin\theta\sigma^y$, $R^\dagger_z(\theta)\sigma^y R_z(\theta) \to \cos\theta\sigma^y + \sin\theta\sigma^x$, we can create sign difference in the X and Y coupling terms if we apply the $R_z(\pi)$ pulse alternating on the sites, e.g., odd-numbered and even-numbered spins in the first and second legs, respectively. In order to change the sign of the random disorder term, we apply the $R_x(\pi)$ gate to each of the spins via utilizing $R^\dagger_x(\theta)\sigma^y R_x(\theta) \to \cos\theta\sigma^y - \sin\theta\sigma^z$. Then the gate sequence that we apply to both copies becomes

$$\Pi_{i:\mathrm{odd}} R^z_{1,i} R^x_{1,i} R^x_{1,i+1} R^z_{2,i+1} R^x_{2,i} R^x_{2,i+1}(\pi), \tag{5}$$

where 1 and 2 denote the leg numbers. Equation (5) could be realized via a programmable acousto-optic modulator with multiple laser outputs the frequency differences of which are negligible [68] and high-resolution imaging devices that can provide single-site addressability [67,69].

(v) Apply the $\sigma^z_{1,1}$ gate on the first spin in the second copy.

(vi) Make an interference measurement between final copies $|\psi_{f1}\rangle = U(-\tau)\sigma^z_{1,i}U(\tau)\sigma^z_{1,1}|\psi_j\rangle$ and $|\psi_{f2}\rangle = \sigma^z_{1,1}U(-\tau)\sigma^z_{1,i}U(\tau)|\psi_j\rangle$ in the hard-core boson limit [61,62]. By measuring the swap operator on both copies [61], we can obtain $\mathrm{Tr}\{\rho_{f1}\rho_{f2}\} = |F_j(\tau)|^2$ for each $|\psi_j\rangle$ initial state where $\rho_{f1} = |\psi_{f1}\rangle\langle\psi_{f1}|$. The same measurement could be applied to the copies of the initial state to check if they are identical, $\mathrm{Tr}\{\rho_j^2\} = 1$. The interference measurement scheme has been applied to measure entanglement entropy [62].

(vii) Repeat the measurement protocol for M times with randomly chosen $|\psi_j\rangle$ initial states to obtain $\frac{1}{M}\sum_j |F_j(\tau)|^2$ which is equal to $|F^{\mathrm{ex}}(t)|^2$ up to an error $\lesssim 10^{-2}$ and $\sim 10^{-4}$ in decay and saturation regimes, respectively, for $M \sim 10^2$ Fock states. Figure 6(f) shows the difference between the square of the exact OTOC [Eq. (3)] and $\frac{1}{M}\sum_j^M |F_j(\tau)|^2$ for M randomly chosen Fock states for a system size $L = 6$.

C. The interferometric scheme

We can measure $F(t)$ with the interferometric approach [20], because the measurement of the control spin either in x or y basis provides the real and imaginary parts of the OTOC, respectively. Figure 8 demonstrates the measurement circuit where the control spin needs to be coupled only to the first spin in the ladder. The protocol is as follows.

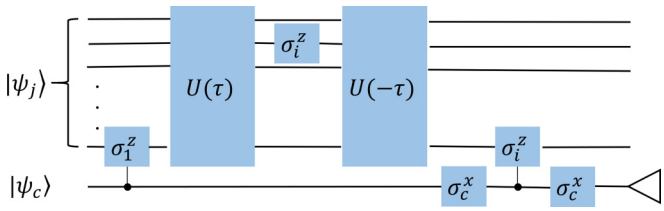

FIG. 8. The measurement circuit for the interferometric approach [20] on the ladder-XX model with local spin observables σ^z_1 and σ^z_i by using an auxiliary spin $|\psi_c\rangle$ to measure only the real part of the OTOC.

(i) Initialize the control spin in a superposition state of $|\psi_c\rangle = (|0\rangle_c + |1\rangle_c)/\sqrt{2}$ to prepare the many-body state

$$\frac{1}{\sqrt{2}}\left[\left(\sigma^z_{1,1}\sigma^z_{1,i}(t)|\psi_j\rangle\right)|0\rangle_c + \left(\sigma^z_{1,i}(t)\sigma^z_{1,1}|\psi_j\rangle\right)|1\rangle_c\right],$$

where the ladder-XX model is simultaneously initiated in a randomly sampled Fock state $|\psi_j\rangle$.

(ii) Apply controlled-σ^z_1 operation to the first spin in the lower leg: $(|0\rangle_c\langle 0| \otimes \mathbb{I}_1 + |1\rangle_c\langle 1| \otimes R^z_{1,1}(\pi)) \otimes \mathbb{I}^{\otimes 2L-1}$.

(iii) Evolve the ladder-XX model forward in time and apply σ^z_i rotation to the spin i: $\mathbb{I}_c \otimes U(\tau)(\mathbb{I}^{\otimes i-1} \otimes \sigma^z_{1,i} \otimes \mathbb{I}^{\otimes 2L-i})$.

(iv) Apply Eq. (5) to the ladder-XX model and evolve the many-body state with $-H$ as $\mathbb{I}_c \otimes U(-\tau)$.

(v) Apply the σ^x_c gate to the control spin before another controlled-σ^z_1 operation, so that we have $(|0\rangle\langle 0|_c \otimes R^z_{1,1}(\pi) + |1\rangle\langle 1|_c \otimes \mathbb{I}_1) \otimes \mathbb{I}^{\otimes 2L-1}$. Further apply another σ^x_c gate to the control spin.

(vi) Make a measurement on the control spin in the x basis to obtain the real part of the OTOC, $\mathrm{Re}[F_j(t)] = \langle\sigma^x_c\rangle = \langle\psi_j(t)|\sigma^x_c|\psi_j(t)\rangle$.

(vii) Repeat the measurement protocol for M times with randomly chosen $|\psi_j\rangle$ initial states to obtain $\frac{1}{M}\sum_j F_j(\tau)$ which is equal to $F^{\mathrm{ex}}(t)$ up to an error shown in Fig. 6.

D. Outlook

The interference measurement scheme requires two copies of the same randomly sampled initial Fock state, which is challenging but doable. On the other hand, the interferometric approach could be realized with only one copy. However, in this measurement scheme we need to couple an auxiliary spin to the first spin and implement controlled-spin gates [70,71], which is challenging in the current technology. Therefore both approaches have certain (dis-)advantages. Important differences that we observe in two measurement schemes are the error bounds due to the measurement output, $|F^{\mathrm{ex}}(t)|^2 = \frac{1}{M}\sum_j^M |F_j(t)|^2$ and $F^{\mathrm{ex}}(t) = \frac{1}{M}\sum_j F_j(t)$ for interference and interferometric, respectively. The error bounds are stable throughout the evolution in the interferometric approach, while they are significantly lower in the saturation regime (by a factor of $\sim 10^2$) and slightly higher in the decay regime of an interference measurement. Therefore, in the case of measuring only the saturation values of the OTOC, the interference measurement seems to be more advantageous.

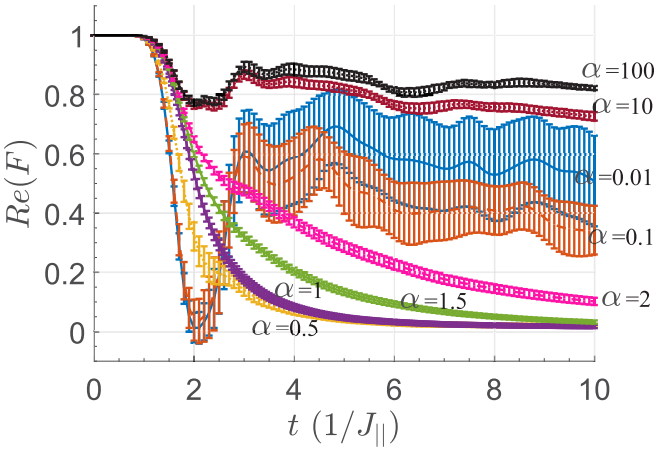

FIG. 9. Error bars of the out-of-time-order correlators with disorder strength of $h = 1\,[J_{||}]$ between two distant operators σ_1^z and σ_7^z with respect to different rung interaction strengths α where $J_\perp = \alpha J_\parallel$ for $L = 7$. The OTOC is averaged over 100 different random samples. The curves are $\alpha = 0.01$ (blue solid), $\alpha = 0.1$ (orange dashed), $\alpha = 0.5$ (yellow dotted), $\alpha = 1$ (purple solid), $\alpha = 1.5$ (green solid), $\alpha = 2$ (pink dashed), $\alpha = 10$ (crimson dotted), and $\alpha = 100$ (black dotted).

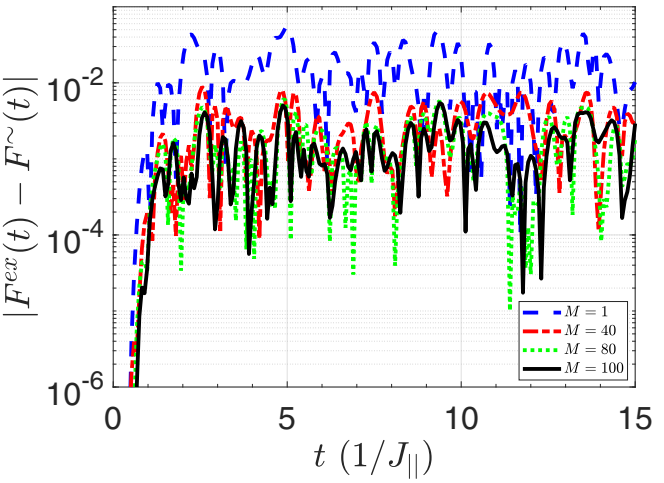

FIG. 10. The difference $|F^{\rm ex}_{i=6}(t) - F^{\sim}_{i=6}(t)|$ for only one Haar-distributed random state (blue dashed), averaged over 40 random states (red dash dotted), 80 states (green dotted), and 100 states (black solid). Only the real part of $F_i^{\sim}(t)$ is taken since the imaginary part is practically zero.

IV. CONCLUSIONS

The ladder-*XX* model's OTOC decay profiles and information spread show a variety of phenomena ranging from quantum chaos to MBL phase and possibly rare-region effects in the ergodic phase that we leave as a future study. We further discussed a Hamiltonian sign reversal protocol that is an alternative to existing approaches in cold atoms and how to apply both interference and interferometric measurements in the scrambling detection with experimental random state preparation. Our results demonstrate that the experiments could utilize only one randomly set Fock state for sufficiently big many-body systems to reproduce infinite-temperature OTOCs up to a bounded error in the chaotic regime. The *XX* ladder has a more convenient experimental cold atom setup compared to the Heisenberg chain, since it lacks *Z*-coupling terms, while it is still interacting due to its quasi-1D nature. Thus, it can be more easily implemented in the laboratory to further investigate scrambling and understand how scrambling changes in the transition from the 1D to 2D case.

ACKNOWLEDGMENTS

This work was supported by the AFOSR Multidisciplinary University Research Initiative program. C.B.D. thanks P. Myles Eugenio for interesting discussions and comments on the paper and on invariant subspaces of the ladder-*XX* models, M. Tran for helpful discussions on superlinear lightcones, and Z.-H. Sun for helpful discussions on the MBL phase in the ladder models.

APPENDIX A: ERROR BARS ON OUT-OF-TIME-ORDER CORRELATORS FOR THE DISORDERED *XX* LADDER

Figure 9 shows the out-of-time-order correlators for different rung couplings with error bars in the case of $h = 1\,[J_{||}]$ random disorder strength. The error bars are significant for smaller rung couplings where the integrable limit of the ladder-*XX* model resides. As the rung coupling becomes equal to intraleg couplings, the error bars become smaller. Therefore, the scrambling that we observe in the chaotic limit is robust to different configurations with the random disorder strength of $h \sim 1\,[J_{||}]$. The error bars are more pronounced in the decay compared to unity and saturation regimes. When we study the opposite regime of the dimer phase where rung coupling is much bigger than the intraleg coupling $\alpha \to \infty$, the error bars do not grow significantly.

APPENDIX B: ERROR BOUNDS ON HAAR-DISTRIBUTED INITIAL STATES

We present the error bounds on the OTOC when Haar random states are used to mimic the $\beta = 0$ initial state in Fig. 10. Figure 10 shows the difference $|F_i^{\rm ex}(t) - F_i^{\sim}(t)|$ for $L = 6$ system size at $h = 1$ random disorder strength with only one random field configuration when $i = 6$ is set. The blue line stands for the case where we take only one random initial state, whereas the black line shows the case where we average over 100 such initial states. The difference is slightly more than an order of magnitude. However, as seen from the other curves, the mixture of a couple of them is quite close to the case with $M = 100$. While using only one random state approximates the OTOC with an error up to 10^{-2}, one can improve the error bound via averaging over only a few states. The results are obtained in this paper with an average of 100 random states.

APPENDIX C: THE EXPONENTIAL AND POWER-LAW FITTING PARAMETERS

Here we present the additional figures and fitting data that show the exponential and power-law decays. Figures 11(a) and 11(b) are for $L = 7$ system size.

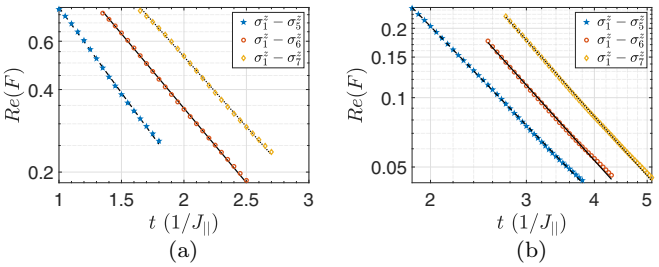

FIG. 11. (a) Semilogarithmic plot for σ_1^z with σ_5^z (blue pentagrams), σ_6^z (red circles), and σ_7^z (orange diamonds) observables in a system size of $L = 7$. The Lyapunov-like exponents follow as 1.4342 ($R^2 = 0.9989$), 1.2507 ($R^2 = 0.9996$), and 1.1767 ($R^2 = 0.9994$) for σ_5^z–σ_7^z with dashed, solid, and dotted lines, respectively. (b) Logarithmic plot for σ_1^z with σ_5^z (blue pentagrams), σ_6^z (red circles), and σ_7^z (orange diamonds) observables in a system size of $L = 7$. The power-law exponents follow as 2.4335 ($R^2 = 0.9999$), 2.6165 ($R^2 = 0.9991$), and 2.6565 ($R^2 = 0.9997$) for σ_5^z–σ_7^z with dashed, solid, and dotted lines, respectively. The data are averaged over 100 different realizations of the Hamiltonian at $h = 1\,[J_{||}]$ for both subfigures.

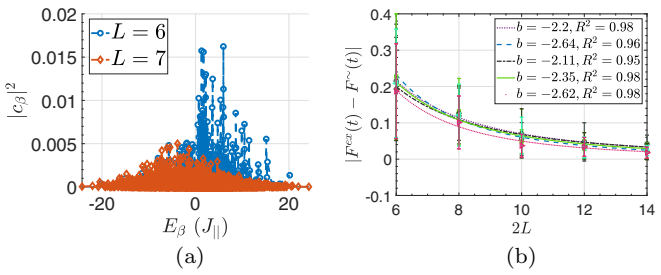

FIG. 12. (a) The EON (eigenstate occupation number) distributions $|c_\beta|^2$ with respect to eigenenergies E_β for $L = 6$ (blue) and $L = 7$ (orange) sizes when only one Fock state is randomly set. (b) The scaling of the mean of the error $|F^{\rm ex}(t) - \frac{1}{M}\sum_j F_j(t)|$ with the system size when we use only one randomly sampled Fock state. Different curves are different random realizations with the legend showing the exponent of the corresponding power-law decay. The error bars stand for 1σ standard deviation around the mean of the error signal.

The Lyapunov-like exponents for $L = 8$ are 1.362 ($R^2 = 0.9986$), 1.229 ($R^2 = 0.9992$), 1.09 ($R^2 = 0.9997$), and 1.015 ($R^2 = 0.9996$) for σ_5^z–σ_8^z, respectively (the figure is shown in the main text). The power-law exponents are 2.1865 ($R^2 = 0.9996$), 2.5506 ($R^2 = 0.9981$), 2.5751 ($R^2 = 0.9976$), and 2.7636 ($R^2 = 0.9995$) for σ_5^z–σ_8^z, respectively. The data are averaged over ten different random samples all at $h = 1$. We also note that the interval of data used for exponential fitting when $L = 8$ is from the time when the OTOC starts to deviate from unity through $t \sim 2\,[1/J_{||}]$, $t \sim 3\,[1/\mathrm{J}]$, $t \sim 4\,[1/J_{||}]$, and $t \sim 4\,[1/J_{||}]$ for σ_5^z, σ_6^z, σ_7^z, and σ_8^z, respectively. The power-law fitting is applied to data seen in Fig. 2(b) (in main text) until $t \sim 5\,[1/J_{||}]$, $t \sim 5\,[1/J_{||}]$, $t \sim 6\,[1/J_{||}]$, and $t \sim 6\,[1/J_{||}]$ for σ_5^z, σ_6^z, σ_7^z, and σ_8^z, respectively. Similarly, the data used for the power-law in the clean limit, $h = 0$, are shown in Fig. 2(c) in the main text (until $t \sim 10\,[1/J_{||}]$ for all operators). The MBL decay form is applied to all data as seen in Fig. 2(d) in the main text.

APPENDIX D: DETAILS ON THE EXPERIMENTAL INITIAL-STATE PREPARATION

We give the plot that shows EON distribution, $|c_\beta|^2$, for $L = 6$ and 7 in Fig. 12(a) for a randomly set initial Fock state. These distributions should be contrasted with a uniform distribution of an infinite-temperature initial state. Even though they are not uniform, they are still broad distributions, which helps the approximation error to be bounded. As a result, we state that as long as the initial state has a broad distribution in the eigenbasis the exact shape of the distribution is not significant. Hence such an initial state could be used to sufficiently approximate an infinite-temperature OTOC.

Figure 12(b) shows that the error ϵ_1 scales as a power law in the system size when only one Fock state is randomly set. This figure focuses on five realizations that were given in the main text in logarithmic scale. Here we plot the data in linear scale to also demonstrate the error bars. The error bars stand for 1σ deviation around the mean of the error signal in time. Note that the error bars increasingly become smaller as the system size increases, meaning that our initial-state approximation works better not only on average but also throughout the simulation time.

Finally we provide the exact fitting expressions for the exponential and power-law scalings of the mean error in the sampling ratio M/N. The exponential scaling parameters are $a = 0.1218$, $R^2 = 0.9134$ ($N = 3$); $a = 0.043$, $R^2 = 0.933$ ($N = 4$); $a = 0.0132$, $R^2 = 0.884$ ($N = 5$); and $a = 0.004$, $R^2 = 0.962$ ($N = 6$) with very close exponents $b \sim -2.5$. The power-law scaling parameters are $a = 0.0112$, $R^2 = 0.984$ ($N = 3$); $a = 0.0037$, $R^2 = 0.991$ ($N = 4$); $a = 8 \times 10^{-4}$, $R^2 = 0.945$ ($N = 5$); and $a = 3.4 \times 10^{-4}$, $R^2 = 0.981$ ($N = 6$) with very close exponents $b \sim -0.5$.

[1] Y. Sekino and L. Susskind, J. High Energy Phys. 10 (2008) 065.
[2] A. Kitaev, KITP Lectures (2015), http://online.kitp.ucsb.edu/online/entangled15/kitaev/.
[3] S. H. Shenker and D. Stanford, J. High Energy Phys. 03 (2014) 67.
[4] J. Maldacena, S. H. Shenker, and D. Stanford, J. High Energy Phys. 08 (2016) 106.
[5] X. Chen, T. Zhou, D. A. Huse, and E. Fradkin, Ann. Phys. **529**, 1600332 (2016).
[6] B. Swingle and D. Chowdhury, Phys. Rev. B **95**, 060201(R) (2017).
[7] R.-Q. He and Z.-Y. Lu, Phys. Rev. B **95**, 054201 (2017).
[8] Y. Huang, Y.-L. Zhang, and X. Chen, Ann. Phys. **529**, 1600318 (2017).
[9] R. Fan, P. Zhang, H. Shen, and H. Zhai, Sci. Bull. **62**, 707 (2017).
[10] M. Heyl, F. Pollmann, and B. Dóra, Phys. Rev. Lett. **121**, 016801 (2018).

[11] D. J. Luitz and Y. Bar Lev, Phys. Rev. B **96**, 020406(R) (2017).
[12] D. J. Luitz and Y. Bar Lev, Phys. Rev. A **99**, 010105 (2019).
[13] A. Bohrdt, C. B. Mendl, M. Endres, and M. Knap, New J. Phys. **19**, 063001 (2017).
[14] S. Xu and B. Swingle, arXiv:1802.00801.
[15] F. J. Dyson, J. Math. Phys. **3**, 140 (1962).
[16] J. Li, R. Fan, H. Wang, B. Ye, B. Zeng, H. Zhai, X. Peng, and J. Du, Phys. Rev. X **7**, 031011 (2017).
[17] C.-J. Lin and O. I. Motrunich, Phys. Rev. B **97**, 144304 (2018).
[18] C. B. Dağ, K. Sun, and L.-M. Duan, arXiv:1902.05041.
[19] K. Hashimoto, K. Murata, and R. Yoshii, J. High Energy Phys. 10 (2017) 138.
[20] B. Swingle, G. Bentsen, M. Schleier-Smith, and P. Hayden, Phys. Rev. A **94**, 040302(R) (2016).
[21] N. Y. Yao, F. Grusdt, B. Swingle, M. D. Lukin, D. M. Stamper-Kurn, J. E. Moore, and E. A. Demler, arXiv:1607.01801.
[22] G. Zhu, M. Hafezi, and T. Grover, Phys. Rev. A **94**, 062329 (2016).
[23] K. X. Wei, C. Ramanathan, and P. Cappellaro, Phys. Rev. Lett. **120**, 070501 (2018).
[24] N. Y. Halpern, Phys. Rev. A **95**, 012120 (2017).
[25] M. Gärttner, J. G. Bohnet, A. Safavi-Naini, M. L. Wall, J. J. Bollinger, and A. M. Rey, Nat. Phys. **13**, 781 (2017).
[26] K. A. Landsman, C. Figgatt, T. Schuster, N. M. Linke, B. Yoshida, N. Y. Yao, and C. Monroe, Nature **567**, 61 (2019).
[27] I. Bloch, J. Dalibard, and W. Zwerger, Rev. Mod. Phys. **80**, 885 (2008).
[28] A. Polkovnikov, K. Sengupta, A. Silva, and M. Vengalattore, Rev. Mod. Phys. **83**, 863 (2011).
[29] C. Pethick and H. Smith, *Bose-Einstein Condensation in Dilute Gases* (Cambridge University, Cambridge, England, 2002).
[30] W. C. Campbell, J. Mizrahi, Q. Quraishi, C. Senko, D. Hayes, D. Hucul, D. N. Matsukevich, P. Maunz, and C. Monroe, Phys. Rev. Lett. **105**, 090502 (2010).
[31] J. Lim, H.-G. Lee, S. Lee, C.-Y. Park, and J. Ahn, Sci. Rep. **4**, 5867 (2014).
[32] T. Barnes, E. Dagotto, J. Riera, and E. S. Swanson, Phys. Rev. B **47**, 3196 (1993).
[33] S. P. Strong and A. J. Millis, Phys. Rev. Lett. **69**, 2419 (1992).
[34] M. T. Batchelor, X. W. Guan, N. Oelkers, and Z. Tsuboi, Adv. Phys. **56**, 465 (2007).
[35] A. Tribedi and I. Bose, Phys. Rev. A **79**, 012331 (2009).
[36] E. Dagotto and T. M. Rice, Science **271**, 618 (1996).
[37] E. Dagotto, Rep. Prog. Phys. **62**, 1525 (1999).
[38] M. Žnidarič, Phys. Rev. Lett. **110**, 070602 (2013).
[39] D. Jaksch, C. Bruder, J. I. Cirac, C. W. Gardiner, and P. Zoller, Phys. Rev. Lett. **81**, 3108 (1998).
[40] M. Greiner, O. Mandel, T. Esslinger, T. W. Hänsch, and I. Bloch, Nature (London) **415**, 39 (2002).
[41] B. Damski, J. Zakrzewski, L. Santos, P. Zoller, and M. Lewenstein, Phys. Rev. Lett. **91**, 080403 (2003).
[42] L. Fallani, J. E. Lye, V. Guarrera, C. Fort, and M. Inguscio, Phys. Rev. Lett. **98**, 130404 (2007).
[43] E. Jané, G. Vidal, W. Dür, P. Zoller, and J. I. Cirac, arXiv:quant-ph/0207011.
[44] P. Hayden, D. W. Leung, and A. Winter, Commun. Math. Phys. **265**, 95 (2006).
[45] D. J. Luitz and Y. B. Lev, Ann. Phys. **529**, 1600350 (2017).
[46] S. Popescu, A. J. Short, and A. Winter, Nat. Phys. **2**, 754 (2006).
[47] J. Emerson, Y. S. Weinstein, M. Saraceno, S. Lloyd, and D. G. Cory, Science **302**, 2098 (2003).
[48] M. Azzouz, L. Chen, and S. Moukouri, Phys. Rev. B **50**, 6233 (1994).
[49] V. Oganesyan and D. A. Huse, Phys. Rev. B **75**, 155111 (2007).
[50] A. Pal and D. A. Huse, Phys. Rev. B **82**, 174411 (2010).
[51] L. D'Alessio, Y. Kafri, A. Polkovnikov, and M. Rigol, Adv. Phys. **65**, 239 (2016).
[52] I. Kukuljan, S. Grozdanov, and T. Prosen, Phys. Rev. B **96**, 060301(R) (2017).
[53] S. Ray, S. Sinha, and K. Sengupta, Phys. Rev. A **98**, 053631 (2018).
[54] T. Iadecola and M. Znidaric, arXiv:1811.07903.
[55] K. Agarwal, E. Altman, E. Demler, S. Gopalakrishnan, D. A. Huse, and M. Knap, Ann. Phys. **529**, 1600326 (2017).
[56] P. Hauke and L. Tagliacozzo, Phys. Rev. Lett. **111**, 207202 (2013).
[57] J. Eisert, M. van den Worm, S. R. Manmana, and M. Kastner, Phys. Rev. Lett. **111**, 260401 (2013).
[58] M. Mezei and D. Stanford, J. High Energy Phys. 05 (2017) 65.
[59] T. S. Nunner and T. Kopp, Phys. Rev. B **69**, 104419 (2004).
[60] S. Sahu, S. Xu, and B. Swingle, arXiv:1807.06086.
[61] A. J. Daley, H. Pichler, J. Schachenmayer, and P. Zoller, Phys. Rev. Lett. **109**, 020505 (2012).
[62] R. Islam, R. Ma, P. M. Preiss, M. E. Tai, A. Lukin, M. Rispoli, and M. Greiner, Nature (London) **528**, 77 (2015).
[63] C. B. Dağ, S.-T. Wang, and L. M. Duan, Phys. Rev. A **97**, 023603 (2018).
[64] A. J. Short, New J. Phys. **13**, 053009 (2011).
[65] H. Shen, P. Zhang, R. Fan, and H. Zhai, Phys. Rev. B **96**, 054503 (2017).
[66] C. Zhang, S. L. Rolston, and S. Das Sarma, Phys. Rev. A **74**, 042316 (2006).
[67] J. H. Lee, E. Montano, I. H. Deutsch, and P. S. Jessen, Nat. Commun. **4**, 2027 (2013).
[68] M. Aldous, J. Woods, A. Dragomir, R. Roy, and M. Himsworth, Opt. Express **25**, 12830 (2017).
[69] W. S. Bakr, J. I. Gillen, A. Peng, S. Fölling, and M. Greiner, Nature (London) **462**, 74 (2009).
[70] L. Isenhower, E. Urban, X. L. Zhang, A. T. Gill, T. Henage, T. A. Johnson, T. G. Walker, and M. Saffman, Phys. Rev. Lett. **104**, 010503 (2010).
[71] A. M. Kaufman, B. J. Lester, M. Foss-Feig, M. L. Wall, A. M. Rey, and C. A. Regal, Nature (London) **527**, 208 (2015).